

# Eurasian October snow water equivalent: using self-organizing maps to characterize variability and identify relationships to the MJO

Gina R. Henderson,\* Bradford S. Barrett and Kaitlyn South

*Oceanography Department, U.S. Naval Academy, Annapolis, MD, USA*

**ABSTRACT:** Variability in October daily snow water equivalent (SWE) change using self-organizing maps (SOMs) was explored in this study. In addition, connections between October Eurasian daily snow water equivalent change ( $\Delta$ SWE) and the leading mode of atmospheric intra-seasonal variability, the Madden–Julian Oscillation (MJO), were considered. Through this analysis, dipole and tripole patterns of daily  $\Delta$ SWE over Eurasia were identified and were moderately negatively correlated to mid-tropospheric geopotential height anomalies. Additionally, SOM nodes capturing over 91% of October days were found moderately correlated with at least one MJO phase. The majority of correlation coefficients with magnitude above 0.30 were found for MJO phases 4–7, indicating that tropical convective anomalies over the Indian Ocean and Maritime Continent have the most impact on October circulation and snow variability. Furthermore, MJO phases with above-normal frequency were most often found in SOM nodes with positive correlations between their respective 500-hPa height anomalies, while MJO phases with below-normal frequency were most often found in SOM nodes with negative correlations between their respective 500-hPa height anomalies. These correlation patterns provide additional evidence linking the MJO to Eurasian snow variability. These results highlight a new application of SOMs in identifying snow variability throughout Eurasia during the month of October, in addition to providing evidence for tropical modulation of the extratropics on the intra-seasonal timescale.

**KEY WORDS** snow depth; MJO; self-organizing map

*Received 23 July 2015; Revised 19 February 2016; Accepted 22 February 2016*

## 1. Introduction

Terrestrial snow is sensitive to the atmosphere on a range of spatial and temporal scales (Barnett *et al.*, 1989; Henderson and Leathers, 2010; Falarz, 2013; Peng *et al.*, 2013; Thompson and Lees, 2014). As such, connecting surface snow amount to variability in atmospheric circulation remains a challenging but important problem (e.g. Derksen and LeDrew, 2000; Dye, 2002; Xia *et al.*, 2014). Because of its general cooling effect on the land surface, snow has temporally lagged relationships with many important general circulation features. For example, winter snow cover over western Eurasia is inversely correlated to subsequent summer monsoon rainfall over the Indian subcontinent (Bamzai and Shukla, 1999; Wu *et al.*, 2014) via a mechanism that strengthens surface pressures over India, weakens the Somali jet, and even weakens tropical easterlies in the eastern Pacific during periods of enhanced winter snow (Vernekar *et al.*, 1995). Autumn Eurasian snow cover is also well linked to lagged relationships with extratropical circulation. For example, greater snow cover in autumn over Eurasia leads to greater surface cooling which

leads to a stronger Siberian high in winter (Cohen and Entekhabi, 1999). Furthermore, years with above-normal October snow extent over Eurasia also tend to have higher geopotential heights in the high latitudes during the subsequent winter (Cohen *et al.*, 2007). This temporal lag is also seen in general circulation models (Gong *et al.*, 2003; Fletcher *et al.*, 2007; Peings *et al.*, 2012), although the upward-propagating Rossby wave signals seen in observations are not as well reproduced, limiting propagation into the stratosphere (Hardiman *et al.*, 2008; Furtado *et al.*, 2015). Autumn Eurasian snow cover has also been found to be a skillful predictor of upcoming winter North Atlantic Oscillation (NAO) mode (Cohen and Jones, 2011; Tian and Fan, 2015), and similarly, October Eurasian snow cover is strongly positively correlated ( $r=0.8$ ) to both 10-m wind speed and significant wave height over the North Atlantic and adjacent seas (Brands, 2014). A potential physical pathway for this lagged teleconnection, described by Cohen *et al.* (2007), starts with above-normal October snow in Siberia, a condition that favours vertical Rossby wave flux activity that acts to weaken the polar stratospheric vortex (Smith *et al.*, 2011), and in turn via downward stratosphere–troposphere coupling (Baldwin and Dunkerton, 1999), this weakened vortex favours the negative phase of the Arctic Oscillation (AO) (Thompson and Wallace, 1998) in the following winter.

\* Correspondence to: G. R. Henderson, Oceanography Department, U.S. Naval Academy, 572C Holloway Road, Annapolis, MD 21402, USA. E-mail: ghenderson@usna.edu

Despite this well-studied lead–lag mechanism driven by autumn Eurasian snow, comparatively little is known about the forcing for variability of October snow itself. Thus, one of the primary goals of this study was to examine patterns of variability in daily change in snow water equivalent (SWE) and identify regions with similar variability, largely on the synoptic scale. Another goal of this study was to explore how observed variability in daily SWE might be connected to the leading mode of atmospheric intra-seasonal variability, the Madden–Julian Oscillation (MJO) (Madden and Julian, 1971, 1972). The MJO is known to modulate wintertime polarity of the NAO (Cassou, 2008), the Pacific–North American (PNA) pattern (Johnson and Feldstein, 2010), and the AO (Flatau and Kim, 2013), as well as daily changes in Northern Hemisphere (NH) spring snow depth (Barrett *et al.*, 2015) and mid-winter and summer Arctic sea ice concentration variability (Henderson *et al.*, 2014). Hence, the hypothesis tested in this study was that the MJO would also have a signal in variability of October Eurasian SWE changes. As such, studies like this one that connect the MJO to snow variability both offer additional explanation for observed October snow variability and reveal another manner by which the tropics and extratropics are connected. The remainder of this article is organized as follows: data and methods are presented in Section 2, results of self-organizing map (SOM) and MJO analyses are presented in Section 3, and conclusions are presented in Section 4.

## 2. Data and methods

The SOM is a neural-network technique based on machine learning (Kohonen, 1988, 2001; Vesanto and Alhoniemi, 2000). At its most basic function, it projects multi-dimensional input data onto a low, usually two-dimensional space. The SOM is useful because it preserves the neighbourhood relationships of the input data. The process iterates and fine-tunes, hence it is called self-organizing, and similar patterns are mapped onto nearby regions in the two-dimensional space, while dissimilar patterns are placed further apart. The SOM is used widely as a data visualization and mining method for complex data sets, and has become increasingly adopted in the geosciences because its clusters tend to have more physical meaning than other statistical techniques (Liu and Weisberg, 2005). A thorough review of SOM techniques and their applications to meteorology is found in Liu and Weisberg (2011).

To explore variability in October SWE over Eurasia (30°–80°N, 15°W–180°E), daily changes in the SWE product available in the ERA-Interim/Land reanalysis (Balsamo *et al.*, 2011) were calculated for all October days from 1980 to 2010. Although termed ‘snow depth’ in the ERA-Interim download interface (available at <http://apps.ecmwf.int/datasets/data/interim-land/type=an/>), the snow product from ERA-Interim/Land is actually SWE (Balsamo *et al.*, 2015). While snow depth and SWE data sets

have some known limitations (Mudryk *et al.*, 2015), the SWE product in the ERA-Interim/Land reanalysis was found to correlate well both spatially and temporally with other observational and satellite retrieval measures of snow, including outperforming the NASA Modern-Era Retrospective Analysis for Research and Applications (MERRA) SWE product (Mudryk *et al.*, 2015). Furthermore, Brun *et al.* (2013) concluded that the snowfall product in the ERA-Interim reanalysis was ‘very reliable’ (and this snowfall is the primary driver of the SWE variable), and Balsamo *et al.* (2015) found that SWE product in ERA-Interim/Land was highly correlated with observations because it combined high-quality ERA-Interim snowfall with cutting-edge representations of blowing snow and sublimation. Anomalies of daily change in SWE ( $\Delta$ SWE) were calculated for each October day (1980–2010) by subtracting mean daily October  $\Delta$ SWE over the entire period from daily  $\Delta$ SWE. While year-to-year variability in October mean SWE was found over Eurasia (Bulygina *et al.*, 2011) and the NH (Estilow *et al.*, 2015), long-term trends (either decreases or increases) in SWE in October over Eurasia have not been found, supporting use of the entire record (1980–2010) to calculate October mean  $\Delta$ SWE.

In this study, an SOM technique similar to the one outlined in Skific and Francis (2012) was used to quantify SWE variability over Eurasia. First, through linear initialization, reference vectors of  $\Delta$ SWE anomalies were constructed. To do this, both eigenvectors and eigenvalues were found such that the largest eigenvalues were paired with two eigenvectors. These eigenvectors allowed the SOM to fit a neural network to the October  $\Delta$ SWE data. Linear initialization allowed for a predetermined number of weights, which, compared to random initialization, trained the data faster (Skific and Francis, 2012). Second, daily  $\Delta$ SWE was compared to the reference vectors using measurement of Euclidean distance. At this stage, the daily  $\Delta$ SWE anomalies were grouped into nodes according to how small or large the Euclidean space was between the data and the reference vector. The process by which the nodes are filled is sometimes referred to as the updating scheme. The third step involved fine-tuning the nodes through minimizing the mean quantization error. After mean quantization error was calculated and node placement of daily  $\Delta$ SWE adjusted, the training was repeated and the data were once more placed in nodes. This adjustment occurred several times as the nodes went through the process of training. Once the training was completed, which occurred after the specified number of iterations had been applied, final reference vectors were prepared. For this study, we tested the technique sensitivity to training using 10 000 and 20 000 iterations, values selected following Haykin (1994), Cavazos (1999), and the SOM Toolbox guidance available online at <http://www.cis.hut.fi/projects/somtoolbox/documentation/index.shtml>. We found little material difference in the identified patterns between 10 000 and 20 000 iterations. Here, we present results from the SOM technique with 20 000 iterations. At this point, the fourth step, the final

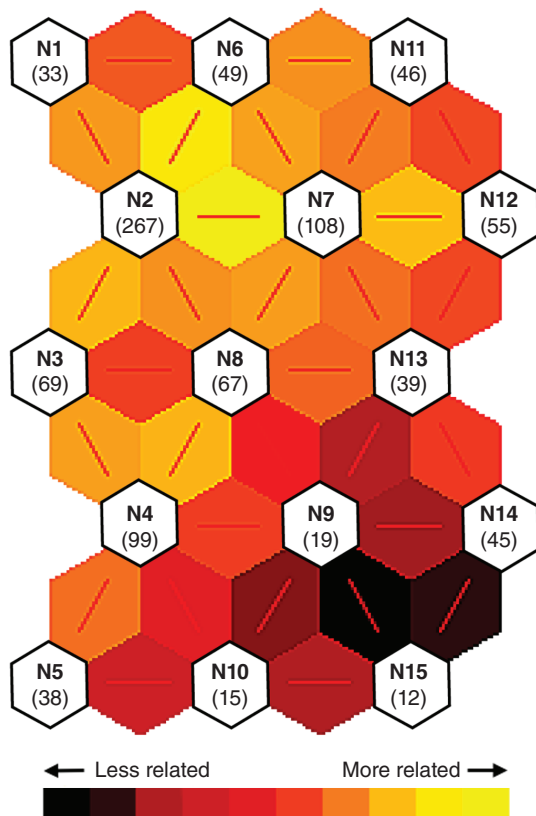


Figure 1. Self-organizing map neural network showing result of clustering Eurasian snow water equivalent for 961 October days (between 1980 and 2010) into 15 nodes. Number of days in each node is given in parentheses. Relative proximity of each neuron's vector weight to its neighbors is indicated by colour shading.

reference vectors were placed on a grid in a similar location as their 'best match' nodes. By the end of this process, daily  $\Delta$ SWE data similar in nature were clustered based in nodes and placed on neural network (Figure 1). Of the 15 nodes, node 2 had the most members (267 October days) and node 15 the fewest members (12 October days). Nodes in the lower-right corner were seen to have weaker relationships between their  $\Delta$ SWE patterns, indicated by darker colours in Figure 1, while nodes in the top left-centre were seen to have more similar  $\Delta$ SWE patterns, indicated by more yellow colours in Figure 1. The nodes with fewer members tended to be least related to each other, while the node with the most members (node 2) was most related to the node with the second-most members (node 7).

Guided by the SOM studies of Richardson *et al.* (2003), Cassano *et al.* (2006), and Blackmore and Goodwin (2008), we selected a neural network with nodes shaped in a  $3 \times 5$  orientation. Through the iterative process of linear initialization, minimizing mean quantization error, and training the data based on a pre-specified number of iterations, daily  $\Delta$ SWE was clustered into similar nodes, thereby identifying patterns that may otherwise have gone unseen if using other compositing techniques (Skific and Francis, 2012). Similar SOM techniques have been used by others to explore snow variability (Cavazos,

2000; Takala *et al.*, 2008; Fassnacht and Derry, 2010), although those studies tended to focus more on regional or catchment basin, not continent-scale variability.

After daily  $\Delta$ SWE anomalies were clustered into nodes by the SOM technique, composite anomalies of  $\Delta$ SWE were calculated for each node by averaging the daily  $\Delta$ SWE anomalies for all of the days in that node. Anomalies of 500-hPa height were calculated for each node by subtracting mean monthly 500-hPa height from the mean daily 500-hPa height for that node. To explore relationships with the MJO, phase and amplitude of the MJO were defined using the daily real-time multivariate MJO (RMM) index (Wheeler and Hendon, 2004). This index is comprised of the two leading principal components (PCs) of a multivariate empirical orthogonal function analysis of daily outgoing longwave radiation and 850- and 200-hPa zonal wind fields. The two PCs classify the phase of MJO, corresponding roughly to the geographical location and intensity of enhanced tropical convection on a particular day (Wheeler and Hendon, 2004). The resulting index describes an MJO cycle that generally progresses eastward, from phase 1 to 8 and back to phase 1 again. Days during which the RMM index had amplitude greater than or equal to 1 (amplitude is defined as the square root of  $RMM1^2 + RMM2^2$ ), and therefore classified as active, were considered for analysis. Days when the RMM index amplitude was less than 1 were considered as inactive and classified as phase 9 for this analysis.

Gridded composite anomalies of 500-hPa height were calculated for each MJO phase at 7-day lags using the following method. First, for each MJO phase, mean 500-hPa heights at day<sub>*n*+7</sub>, which was 7 days after an active MJO day<sub>*n*</sub>, were calculated at each grid point. Mean values included all days that met the active MJO threshold, but no other tests (e.g. eastward propagation, consecutive-day active, etc.) were applied. Second, October (1980–2010) mean 500-hPa heights on day<sub>*n*+7</sub> were subtracted to calculate lagged 500-hPa height anomalies for that phase. Third, daily anomalies of 500-hPa height were averaged for each MJO phase to find the anomaly for that phase. Anomalies were examined at a 7-day lag following Casou (2008), L'Heureux and Higgins (2008), Lin and Brunet (2009), and Flatau and Kim (2013), who found that the NH extratropical response lagged tropical MJO convection by approximately 7 days.

### 3. Results

To give context to SOM-based snow analysis, mean daily  $\Delta$ SWE in October was calculated (Figure 2). Throughout Eurasia, mean daily  $\Delta$ SWE varied from approximately  $0$ – $2.5$  mm day<sup>-1</sup>, with largest changes occurring across north central to northeast Eurasia). Lesser values of daily  $\Delta$ SWE were noted over Europe and western Asia, generally less than  $1$  mm day<sup>-1</sup> in October. Daily  $\Delta$ SWE during this month was generally limited to north of the 50th parallel, with the exception of some higher elevation locations. As will be shown in the results that follow, some nodes of

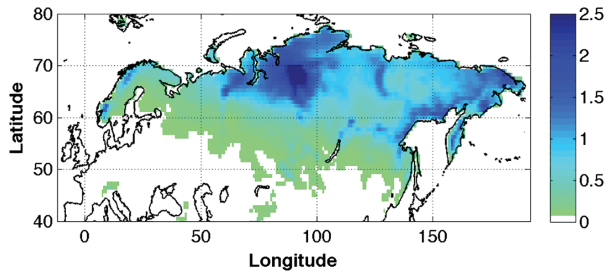


Figure 2. October mean daily snow change ( $\Delta$ SWE), in  $\text{mm day}^{-1}$ , from the ERA-Interim/Land reanalysis, 1980–2010.

snow variability had anomalies well in excess of 100% of the October mean, both over the areas with largest mean  $\Delta$ SWE but also in the western parts of Eurasia, where mean  $\Delta$ SWE often was less than  $1 \text{ mm day}^{-1}$ .

### 3.1. SOM analysis of daily $\Delta$ SWE variability

Several interesting patterns of  $\Delta$ SWE variability emerged from the SOM analysis (Figure 3). First, one node, node 2 (Figure 3(b)), displayed pan-continent variability largely of the same sign (positive, indicated by blue colours). Node 2 was also the node populated by the most days (267). The magnitude of these positive  $\Delta$ SWE values was up to  $3 \text{ mm day}^{-1}$ , indicating that the mean daily  $\Delta$ SWE change on about 20% of the days in October was above normal, particularly so over regions of central and eastern Europe that typically see very little mean  $\Delta$ SWE (Figure 2). Other nodes displayed dipole- and tripole-like patterns of  $\Delta$ SWE variability. For example, node 1 (Figure 3(a)), which represented about 3% of October days, exhibited a tripole positive–negative–positive  $\Delta$ SWE pattern that spanned

Northern Europe, central and north-central Eurasia, and eastern Eurasia. Nodes 3, 4, and 5 (Figure 3(c)–(e)) representing 19% of October days, also exhibited tripole patterns across Europe and Asia, but in those nodes, the negative anomaly centres were located farther west when compared to node 1. Nodes 9, 10, and 15 (Figure 3(i), (j), and (o)), representing 4% of October days, resembled more of a dipole, and especially in nodes 10 and 15, the dipole was oriented more north–south, contrasting with nodes 1, 3, 4, and 5. This contrast is a typical characteristic of SOM node arrangements, whereby nodes located in opposite corners of the neural network tend to be most dissimilar.

To link observed surface  $\Delta$ SWE patterns to atmospheric variability in the middle troposphere, 500-hPa height ( $z500$ ), composited for each SOM node using the same subset of days as the  $\Delta$ SWE field and expressed as anomalies from the mean October 1980–2010  $z500$  field, was examined (Figure 4). Anomalies of  $z500$  were also chosen because an additional goal of this study was to investigate relationships between  $\Delta$ SWE and the MJO, and convective heating like that of the MJO is known to modulate extratropical circulation (Sardeshmukh and Hoskins, 1988; Matthews *et al.*, 2004; Yoo *et al.*, 2012; Barrett *et al.*, 2015) with approximately a 7-day lag (Casou, 2008; L’Heureux and Higgins, 2008; Lin and Brunet, 2009; Flatau and Kim, 2013). Similar to daily  $\Delta$ SWE, anomalies of  $z500$  by node often resembled dipole- and tripole-like patterns (Figure 4). Given that mean October  $z500$  heights over North America were largely zonal (not shown), positive and negative  $z500$  anomalies indicated waviness and implied meridional flow structures. In node 1, positive  $z500$  anomalies centred near  $100^\circ\text{E}$  were

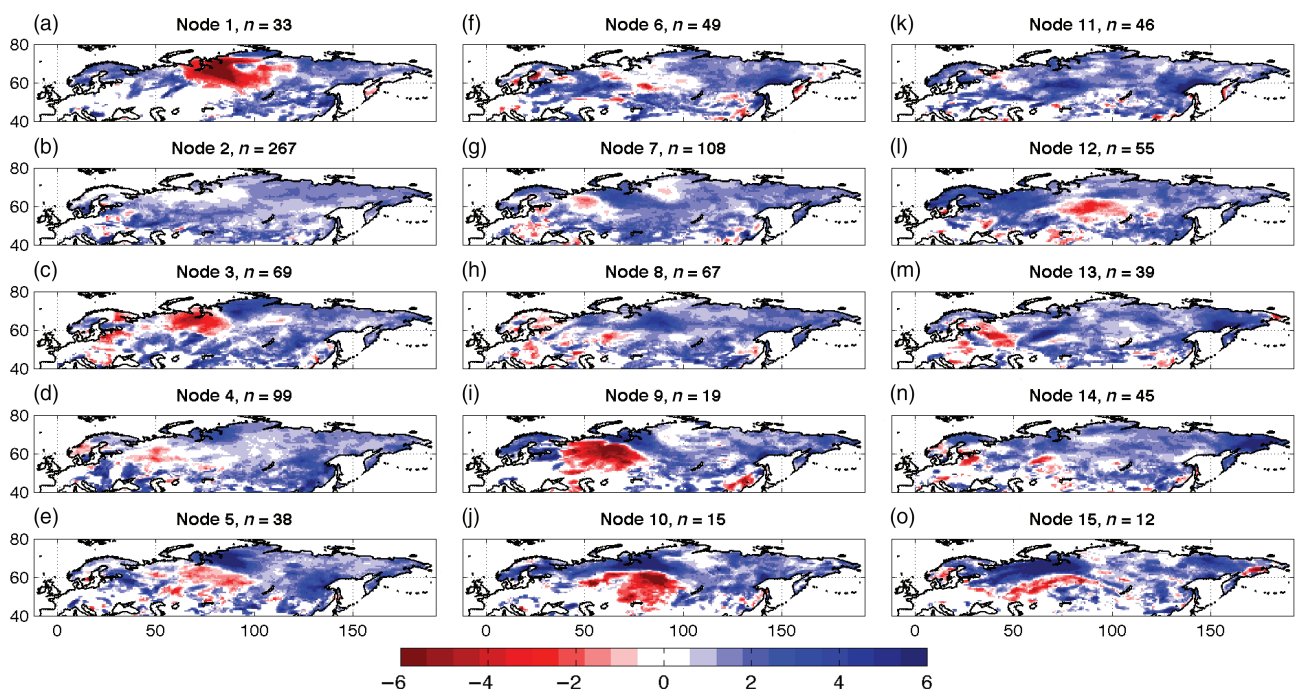


Figure 3. Anomalous mean daily snow change ( $\Delta$ SWE), in  $\text{mm day}^{-1}$ , October 1980–2010, for 15 self-organizing map (SOM) nodes (a–o). Node number and number of days in each node  $n$  are given at top of each panel.

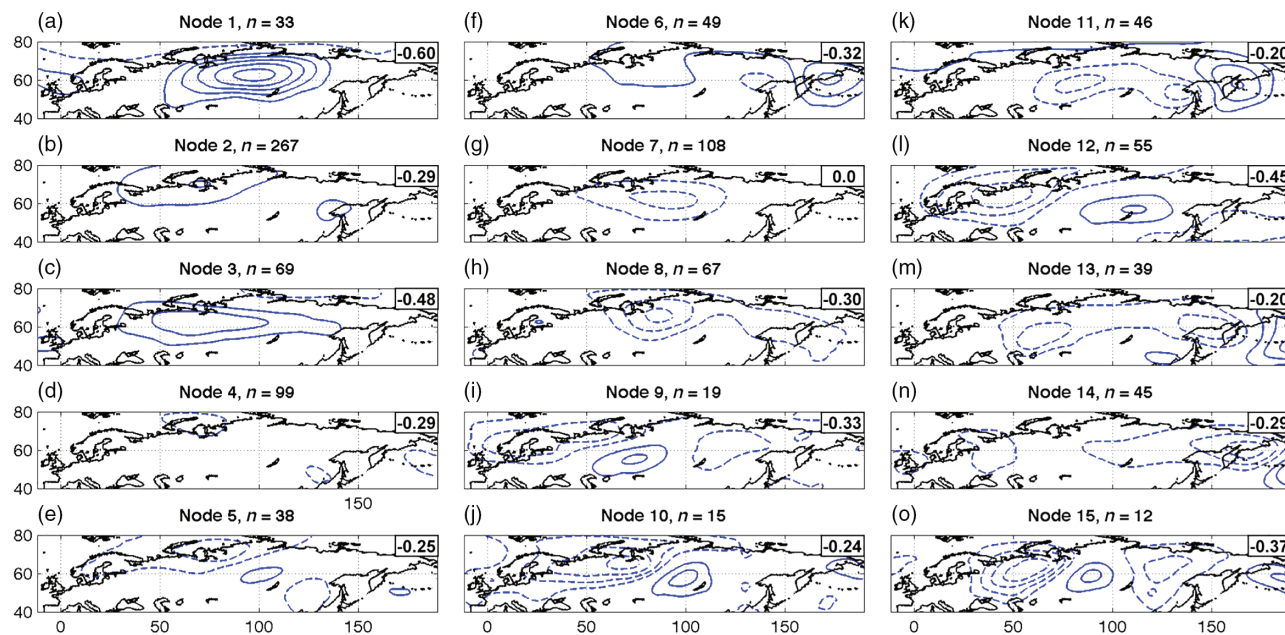


Figure 4. As in Figure 3, but for 500-hPa height ( $z500$ ) anomalies (in m). Positive anomalies indicated by solid contours and negative anomalies by dashed contours, with contour interval of 40 m. Correlation coefficients  $r$  between daily  $z500$  anomalies and daily  $\Delta$ SWE anomalies (Figure 3) given in upper-right corner of each panel. Correlation coefficients for all nodes, with the exception of node 7, were statistically significantly different from zero with 99% confidence.

flanked on either side by negative anomalies, indicating a trough-ridge-trough circulation pattern, also known as an omega block (Figure 4(a)). Similar positive height anomalies were seen in nodes 2 and 3, although the positive anomaly centres were found shifted west to near  $70^\circ\text{E}$  (Figure 4(b) and (c)). Other nodes featured negative  $z500$  anomalies over Europe or central Eurasia and positive anomalies to the east, including nodes 11, 12, and 13 (Figure 4(k)–(m)). Tripole  $z500$  anomalies were seen in node 5 (Figure 4(e)), nodes 9, 10, and 15 (Figure 4(i), (j), and (o)).

The  $z500$  anomalies agreed qualitatively with  $\Delta$ SWE anomalies for many nodes, in that ridges (troughs) were collocated with regions of negative (positive)  $\Delta$ SWE anomalies. To quantify the strength of this agreement between  $z500$  anomalies and  $\Delta$ SWE anomalies, Pearson product–moment correlation coefficients between the two fields were calculated for each node. Correlation values are reported in the upper-right corner of panels in Figure 4. Statistically significant (at the 99% confidence level using a Student’s  $t$ -test for correlation coefficients) correlations between 500 hPa height anomalies and anomalies in daily change in SWE were found for all nodes except node 7. Strongest correlations were found for node 1 ( $r = -0.60$ ) and node 3 ( $r = -0.48$ ). In those two nodes, which represent about 10% of October days, negative  $\Delta$ SWE anomalies over north-central Asia were seen generally collocated with positive  $z500$  anomalies. This was not surprising, as mid-tropospheric ridges tend to be associated with clearer skies and warmer temperatures, which would be associated with below-normal (negative)  $\Delta$ SWE. In node 12 ( $r = -0.45$ ), which featured a pronounced dipole in  $z500$  anomalies, negative height

anomalies over Europe were collocated with positive  $\Delta$ SWE anomalies there, while positive height anomalies along  $60^\circ\text{N}$  between  $100^\circ$  and  $150^\circ\text{E}$  were generally collocated with negative  $\Delta$ SWE anomalies. Physically, in node 12, mid-tropospheric troughs (represented as negative  $z500$  height anomalies) can be associated with both precipitation and below-normal temperatures, both of which would support the observed above-normal (positive)  $\Delta$ SWE anomalies. Even those nodes with correlation coefficients  $r$  between  $-0.30$  and  $-0.40$ ,  $z500$  anomalies were generally collocated with the opposite-signed  $\Delta$ SWE anomalies. However, it is possible that the correlation coefficients were lower in those nodes because of the baroclinic nature of the atmosphere in October, whereby anomaly centres of mid-troposphere  $z500$  and surface  $\Delta$ SWE would not vertically align, thus reducing the correlations between the two fields. It is also possible that other factors, besides simply snowfall or snow melt, including snow compaction, snowpack metamorphosis, or blowing snow, also influenced  $\Delta$ SWE and led to weaker correlations with  $z500$  heights. Despite such factors, these correlations agreed well with Barrett *et al.* (2015), who found similar agreement between  $\Delta$ SWE and  $z500$  in spring (March–May).

### 3.2. Connection to the MJO

To test possible relationships between October daily  $\Delta$ SWE variability and the MJO,  $z500$  height anomalies lagged by 7 days were calculated for each active MJO phase (and also for the inactive neutral phase). These anomalies were then correlated with  $z500$  height anomalies for each SOM node. Approximately 56% of days featured active MJO, and approximately 44% of those days were inactive (Figure 5), statistics supported by

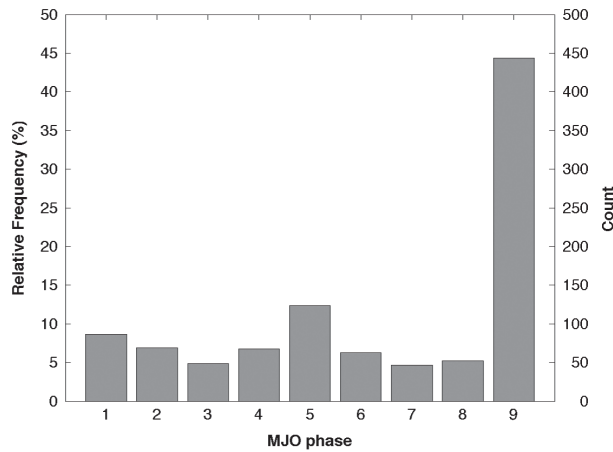


Figure 5. Relative frequency (left axis) and number of days (right axis) of each active phase 1–8, with non-active (neutral) MJO indicated as phase 9, October 1980–2010.

the MJO climatology of LaFleur *et al.* (2015). Among the eight active phases, days were somewhat unevenly distributed amongst MJO phases 1–8, where phases 5 and 1 occurred most often (Figure 5), with approximately 12 and 8% relative frequency (Figure 5), while phases 3 and 7 occurred least often (Figure 5), each with approximately 5% of the days in the period (Figure 5).

Composite anomalies of z500 were calculated at 7-day lags for each active MJO phase as well as the neutral phase (Figure 6). For each active phase, height anomalies were seen over much of Eurasia. For example, 7 days after active phases 1 and 3, negative z500 anomalies were found extending across all of northern Eurasia, with positive anomaly centres near 60° and 150°E (Figure 6(a) and (c)). Height anomalies 7 days after active phases 2 and 7 resembled wave trains: in phase 2, negative–positive–negative–positive centres spread across all of Eurasia (Figure 6(b)), and in phase 7, a positive–negative–positive train of anomalies was seen (Figure 6(g)). Seven days after neutral MJO, z500 height anomalies tended towards zero (Figure 6(i)).

Some similarity was noted between z500 anomaly patterns in the SOM node composites and patterns in the

lagged MJO phases. For example, for many MJO phases and SOM nodes, z500 anomalies were of synoptic scale, with positive and negative anomaly centres separated by between 1000 and 2000 km. Additionally, the magnitude of height anomalies by MJO phase sometimes approached those seen in the SOM nodes, although for most MJO phases, z500 anomaly magnitudes were smaller than z500 magnitudes for SOM nodes (and the contour interval in Figure 6 is 20 m, only 50% of the contour interval in Figure 4). Nevertheless, these similarities suggested a potential modulation of mid-troposphere circulation by the MJO. To test the degree of spatial similarity between the two z500 anomaly fields, Pearson product–moment correlation coefficients were calculated (Table 1) between the z500 anomalies for each SOM node (Figure 4) and the z500 anomalies for each MJO phase (Figure 6). Statistical significance at the 99% confidence level was calculated using the Student's *t*-test for correlation coefficients. Given the large number of grid points in each field, most of the correlations between SOM and MJO z500 were statistically significantly different from zero. Thus, to aid in identifying potentially physically meaningful correlations,  $|r| > 0.30$  was selected as a threshold. Of the 120 correlation coefficients between 15 SOM nodes and 8 active MJO phases, 39 (or 32.5%) met this threshold. With the exception of nodes 6 and 14, all other nodes, representing 91% of October days, had at least one correlation magnitude above 0.30. This strongly suggests at least some role of the MJO in modulating mid-troposphere circulation in October. The largest positive correlations were seen between node 12 and phase 4 ( $r = 0.61$ ) and node 4 and phase 8 ( $r = 0.58$ ), and six other node–phase correlations featured coefficients above 0.50. The largest negative correlations were seen between node 2 and phase 6 ( $r = -0.69$ ) and also between node 3 and phase 5 ( $r = -0.64$ ), and two other node–phase correlations featured coefficients more negative than  $-0.50$ .

Physically, the strongest positive correlation suggests that the October 500-hPa height field over Eurasia 7 days after enhanced convection over the Maritime Continent (the geographical location of MJO phase 4) most closely

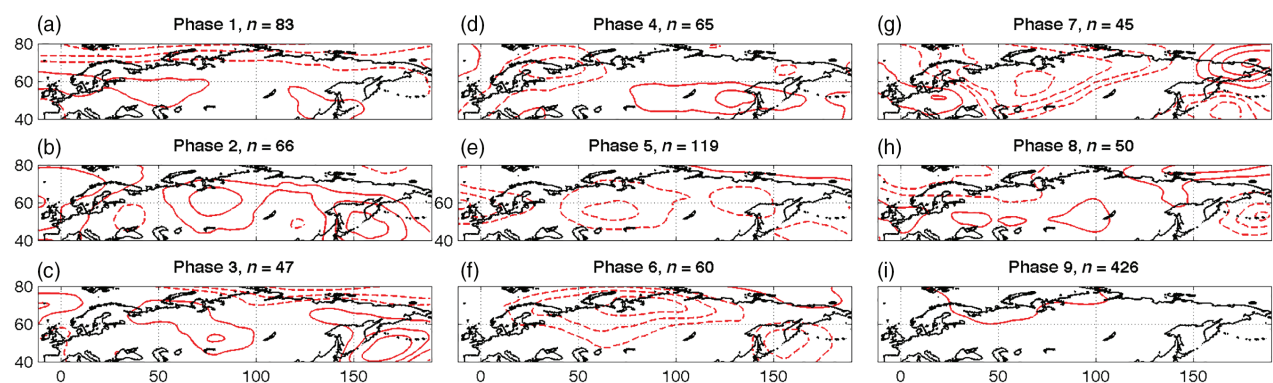


Figure 6. Anomalies of z500 (in m) for October 1980–2010 for eight active MJO phases 1–8 (a–h), with and non-active (neutral) MJO phase 9 (i). As in Figure 4, positive anomalies indicated by solid contours and negative anomalies by dashed contours, with contour interval of 20 m. Number of days in each phase  $n$  is given at the top of each panel.

Table 1. Pearson product–moment correlation coefficients between 500-hPa height anomalies by SOM node and 500-hPa height anomalies by MJO phase.

	Phase 1	Phase 2	Phase 3	Phase 4	Phase 5	Phase 6	Phase 7	Phase 8
Node 1	<b>0.49<sup>+</sup></b>	<b>0.24</b>	<b>0.20</b>	<b>0.27</b>	<b>−0.48<sup>−</sup></b>	<b>−0.41<sup>−</sup></b>	<b>−0.28</b>	<b>0.31<sup>+</sup></b>
Node 2	<b>−0.14</b>	<b>0.08</b>	<b>0.04</b>	<b>−0.34<sup>−</sup></b>	<b>−0.19</b>	<b>−0.69<sup>−</sup></b>	<b>−0.58<sup>−</sup></b>	<b>−0.22</b>
Node 3	<b>0.52<sup>+</sup></b>	<b>0.27</b>	<b>0.27</b>	<b>−0.10</b>	<b>−0.64<sup>−</sup></b>	<b>−0.56<sup>−</sup></b>	<b>−0.53<sup>−</sup></b>	<b>0.04</b>
Node 4	0.01	<b>−0.11</b>	<b>−0.26</b>	<b>−0.28</b>	<b>0.06</b>	<b>0.21</b>	<b>0.11</b>	<b>0.58<sup>+</sup></b>
Node 5	<b>0.25</b>	<b>0.14</b>	<b>0.32<sup>+</sup></b>	<b>0.37<sup>+</sup></b>	0.00	<b>0.30<sup>+</sup></b>	<b>0.32<sup>+</sup></b>	<b>0.15</b>
Node 6	<b>−0.25</b>	<b>−0.09</b>	<b>0.03</b>	<b>−0.14</b>	<b>0.28</b>	<b>−0.15</b>	0.01	<b>−0.11</b>
Node 7	<b>−0.17</b>	<b>−0.09</b>	<b>−0.14</b>	0.00	<b>0.22</b>	<b>0.50<sup>+</sup></b>	<b>0.44<sup>+</sup></b>	<b>−0.18</b>
Node 8	<b>0.19</b>	<b>−0.40</b>	<b>−0.17</b>	<b>−0.15</b>	<b>0.19</b>	<b>0.56<sup>+</sup></b>	<b>0.33<sup>+</sup></b>	<b>−0.03</b>
Node 9	<b>0.22</b>	−0.01	0.00	<b>0.54<sup>+</sup></b>	<b>−0.02</b>	<b>0.16</b>	<b>−0.03</b>	<b>0.29</b>
Node 10	<b>0.03</b>	<b>−0.11</b>	0.00	<b>0.55<sup>+</sup></b>	<b>0.29</b>	<b>0.52<sup>+</sup></b>	<b>0.51<sup>+</sup></b>	<b>0.29</b>
Node 11	<b>−0.44<sup>−</sup></b>	<b>0.09</b>	<b>0.07</b>	<b>−0.35<sup>−</sup></b>	<b>0.33<sup>+</sup></b>	<b>0.09</b>	<b>0.28</b>	<b>−0.33<sup>−</sup></b>
Node 12	<b>0.04</b>	<b>−0.04</b>	<b>−0.08</b>	<b>0.61<sup>+</sup></b>	<b>0.05</b>	<b>0.46<sup>+</sup></b>	<b>0.44<sup>+</sup></b>	<b>0.40<sup>+</sup></b>
Node 13	<b>−0.16</b>	<b>−0.20</b>	<b>−0.08</b>	<b>0.06</b>	<b>0.38<sup>+</sup></b>	<b>0.46<sup>+</sup></b>	<b>0.45<sup>+</sup></b>	<b>−0.31<sup>−</sup></b>
Node 14	<b>−0.26</b>	<b>−0.04</b>	<b>−0.17</b>	<b>0.12</b>	<b>0.15</b>	<b>0.07</b>	<b>−0.28</b>	<b>−0.16</b>
Node 15	<b>−0.15</b>	<b>0.19</b>	<b>0.02</b>	<b>0.31<sup>+</sup></b>	<b>0.21</b>	<b>0.28</b>	<b>0.33<sup>+</sup></b>	<b>−0.02</b>

Bold values indicate coefficients statistically significant from zero with 99% confidence. Symbols indicate strongest correlation coefficients, above 0.30 (+) and below −0.30 (−), also shown in Figure 7.

resembles that of node 12. The strongest negative correlation suggests that the height field over Eurasia 7 days after enhanced convection over the Western Pacific (the location of MJO phase 6) would be opposite of the height field of node 2. In addition to these physical relationships, several other interesting patterns emerged in the correlations. For example, the majority of the correlation coefficients with magnitude above 0.30 were found for MJO phases 4–7. Per the Wheeler and Hendon (2004) definitions, these four phases are located geographically closest to Eurasia. This result suggests that those four MJO phases cumulatively have the most impacts on mid-troposphere circulation. Another interesting pattern that emerged in the correlations was how the coefficients were distributed among the SOM nodes. In phases 4–7, positive correlations were found with higher numbered nodes and negative correlations were found with lower numbered nodes. The self-similarity among low-numbered nodes and high-numbered nodes, and the differences between low- and high-numbered nodes, agrees well with the SOM neural network construction (Figure 1): similar nodes were located closer together and dissimilar nodes located farther apart. This pattern was also seen for MJO phases 1 and 8, with positive correlations seen with lower numbered SOM nodes and negative correlations with higher numbered SOM nodes. Finally, differences in correlations between MJO phases were also seen. For example, in low-numbered SOM nodes (e.g. nodes 1–3), positive correlations were seen with MJO phases 1 and 8 and negative correlations with phases 4–7. Similarly, in higher numbered SOM nodes (e.g. nodes 9–11), negative correlations were seen with MJO phases 1 and 8 and positive correlations were seen with MJO phases 4–7. The similarity between phases 1 and 8 and phases 4–7 agrees well with the geographic regions defined by Wheeler and Hendon (2004), whereby numbered MJO phases correspond roughly to geographic zones that progress eastward with number (and wrapping around between phases 8 and 1).

To further explore the variability of MJO phases in each SOM node, anomalous relative frequencies in the occurrence of each phase (calculated with respect to the October 1980–2010 mean) were calculated for each SOM node (Figure 7). What emerged was another indication of MJO influence on z500 heights for most patterns of snow variability. For example, for most nodes, MJO phases that were positively correlated with mid-tropospheric height (indicated by red plus symbols in Figure 7) were found for nodes that occurred more frequently than the October mean. Similarly, MJO phases that were negatively correlated with mid-tropospheric height (indicated with green minus symbols in Figure 7) were found for nodes that occurred less frequently than normal. To better understand this pattern, three nodes were analysed in detail: nodes 1, 3, and 12, representing 14.5% of October days. Those three nodes were selected because they had the greatest correlations between node  $\Delta$ SWE anomalies (Figure 3) and node z500 anomalies (Figure 4). Nodes 1 and 3 both featured a region of negative  $\Delta$ SWE over northwest Eurasia centred near 65°N (Figure 8(a) and (f)), and both nodes featured a region of positive z500 anomalies nearly in the same region. However, both nodes also featured a region of negative z500 anomalies extending across nearly all of Eurasia poleward of about 70°N. It is likely that region of negative z500 anomalies (along with the weak but positive anomalies seen near 60°N) supported the moderate correlations ( $r = +0.49$  and  $r = +0.52$ , respectively) seen between z500 of nodes 1 and 3 and z500 of phase 1 (Table 1). MJO phase 1 occurred with above-normal frequency in both nodes 1 and 3 (Figure 8(e) and (j)), supporting the conclusion that the MJO exerts influence in the circulation and snow patterns of those two nodes. Additionally, z500 heights 7 days after active MJO phase 5 were most strongly negatively correlated with z500 heights for nodes 1 and 3 ( $r = -0.48$  and  $r = -0.64$ , respectively). These negative correlations were likely the result of the negative z500 anomalies seen over much of Europe after MJO phase 5

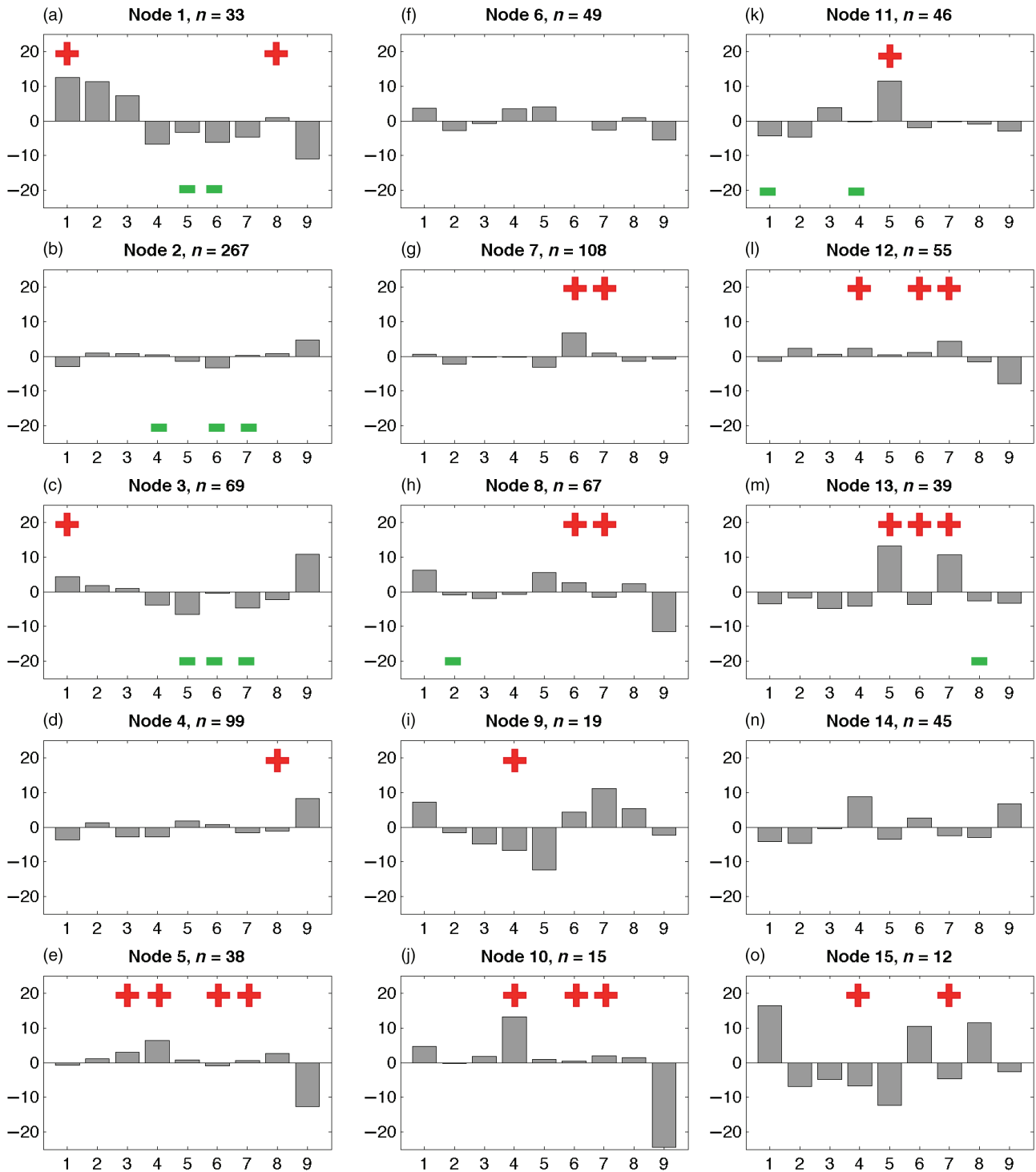


Figure 7. Relative frequency anomalies of each active MJO phase 1–8 and neutral MJO phase 9 (phases indicated on the abscissa axes) for each SOM node (a–o). MJO relative frequency anomalies expressed with respect to the October 1980–2010 mean found in Figure 5. Red + and green symbols indicate anomalies where correlation coefficients of z500 anomalies (found in Table 1) were above 0.30 (+) or below -0.30 (-). Number of days in each node  $n$  is given at the top of each panel.

(Figure 8(d) and (i)). Similar to phase 1, phase 5 occurred less frequently than average in both node 1 and node 3. Finally, in node 12, a tripole positive–negative–positive snow pattern was seen (Figure 8(k)), and an accompanying negative–positive–negative z500 height pattern was also seen (Figure 8(l)). Two MJO phases were found to

have z500 anomalies most positively correlated to node 12 z500 anomalies: phases 4 and 7, and those two phases occurred more frequently in node 12 than the October mean. Thus, similar to nodes 1 and 3, these results support the conclusion that the MJO influenced the circulation and snow patterns represented by node 12.

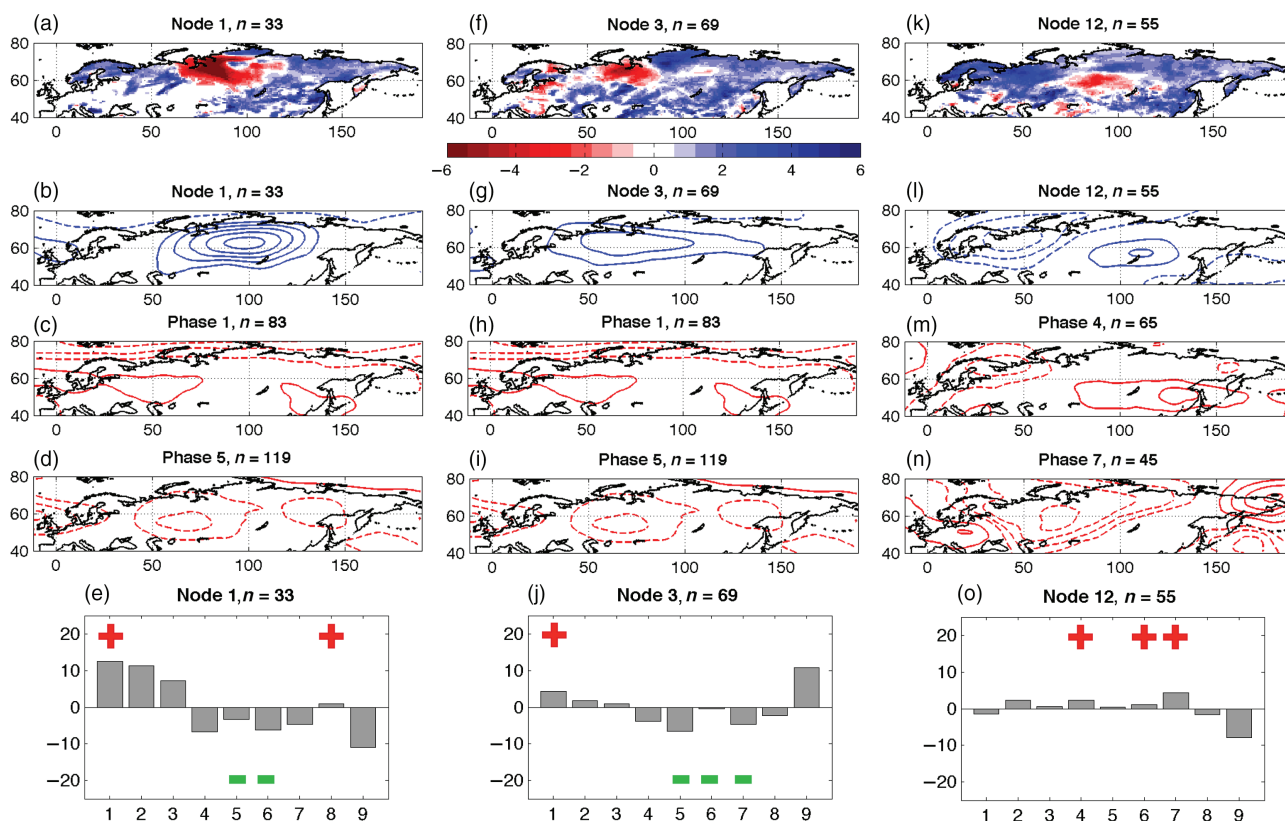


Figure 8. Mean daily  $\Delta$ SWE anomalies (in  $\text{mm day}^{-1}$ , a, f, and k) and z500 anomalies (in m, contour interval 40 m; b, g, and l) for nodes 1, 3, and 12, nodes selected for having strongest correlations between  $\Delta$ SWE and z500. Mean daily z500 anomalies (in m, contour interval 20 m; c, d, h, i, m, and n) for MJO phases 1, 5, 4, and 7, respectively, selected for having strongest correlations to node z500 anomalies. Anomalies of relative frequency of MJO phases (e, j, and o) for nodes 1, 3, and 12. Plus and minus symbols indicate phases with strongest positive and negative correlations between MJO z500 and node z500 anomalies.

#### 4. Summary and conclusions

Motivated by the well-studied lead–lag relationship between autumn snow and subsequent winter NH circulation, and by the comparative lack of previous work on autumn snow variability, this article sought to examine patterns of variability in October SWE over Eurasia. This was achieved using SOMs, a method which has been increasingly adopted in the geosciences. In addition, connections between October Eurasian  $\Delta$ SWE to the leading mode of atmospheric intra-seasonal variability, the MJO, were explored.

The principal findings of the current study are as follows. (1) Fifteen patterns of large-scale October  $\Delta$ SWE variability were identified over Eurasia. Most of these patterns showed coherent regions of synoptic-scale  $\Delta$ SWE variability, ranging from predominantly positive daily  $\Delta$ SWE across Eurasia to dipole- and tripole-like patterns of  $\Delta$ SWE variability. (2) SOM patterns of daily  $\Delta$ SWE variability were found moderately correlated to anomalies of mid-tropospheric geopotential height. Physical organization of daily  $\Delta$ SWE and z500 anomalies consistently showed positive (negative) daily  $\Delta$ SWE anomalies being collocated with mid-tropospheric negative (positive) z500 anomalies. (3) The majority of correlation coefficients with magnitude above 0.30 were found for MJO phases 4–7, indicating that tropical convective anomalies over

the Indian Ocean and Maritime Continent have the most impact on October circulation and snow variability. (4) Correlations with mid-troposphere height anomalies differed between lower numbered and higher numbered SOM nodes, agreeing well with the statistical construction of the SOM node array. Additionally, differences in correlation coefficient signs were seen between MJO phases 1 and 8 and phases 4–7, in agreement with the geography and eastward progression of MJO phases. (5) Positive correlations of 500-hPa height were most often seen for MJO phases that occurred with above-normal frequency in those nodes, and negative correlations were most often seen for MJO phases that occurred with below-normal frequency in those nodes. This relationship was seen particularly for nodes 1, 3, and 12, providing additional evidence for MJO modulation of Eurasian snow variability represented by those three nodes.

The results presented in this article highlight a new application of SOMs in identifying snow variability in Eurasia during the month of October. Correlations between  $\Delta$ SWE and z500 heights agreed well with previous studies of spring  $\Delta$ SWE variability (Barrett *et al.*, 2015). In addition, the hypothesis that the MJO would have a signal with October  $\Delta$ SWE was explored and validated for some patterns of  $\Delta$ SWE variability and MJO phases 4–7, likely for the first time providing evidence for the relationship between autumn Eurasia snow variability and tropical

convection. This study therefore provides additional evidence for connections between the tropics and the extratropics on intra-seasonal timescales.

## Acknowledgements

This work was partially sponsored by National Science Foundation award PLR-12-3843. The authors thank the helpful comments and feedback from the two anonymous reviewers.

## References

- Baldwin MP, Dunkerton TJ. 1999. Propagation of the Arctic Oscillation from the stratosphere to the troposphere. *J. Geophys. Res. Atmos.* **104**: 30937–30946.
- Balsamo G, Boussetta S, Dutra E, Beljaars A, Viterbo P, van den Hurk B. 2011. Evolution of land surface processes in the IFS. *ECMWF Newsl* **127**: 17–22.
- Balsamo G, Albergel C, Beljaars A, Boussetta S, Brun E, Cloke H, Dee D, Dutra E, Muñoz-Sabater J, Pappenberger F, de Rosnay P, Stockdale T, Vitart F. 2015. ERA-interim/land: a global land surface reanalysis data set. *Hydrol. Earth Syst. Sci.* **19**: 389–407.
- Banzai AS, Shukla J. 1999. Relation between Eurasian snow cover, snow depth, and the Indian summer monsoon: an observational study. *J. Clim.* **12**: 3117–3132.
- Barnett TP, Dumenil L, Schlese V, Roeckner E, Latif M. 1989. The effect of Eurasian snow cover on regional and global climate variations. *J. Atmos. Sci.* **46**: 661–685.
- Barrett BS, Henderson GR, Werling JS. 2015. The influence of MJO on the intraseasonal variability of Northern Hemisphere spring snow depth. *J. Clim.* **28**: 7250–7262, doi: 10.1175/JCLI-D-15-0092.1.
- Blackmore KL, Goodwin ID. 2008. Climate variability of the Hunter, Lower North Coast and Central Coast Region of NSW. Consultancy Report by Newcastle Innovation for the Hunter and Central Coast Regional Environment Management Strategy (HCCREMS), HCCREMS, 1–91.
- Brands S. 2014. Predicting average wintertime wind and wave conditions in the North Atlantic sector from Eurasian snow cover in October. *Environ. Res. Lett.* **9**: 045006.
- Brun E, Vionnet V, Boone A, Decharme B, Peings Y, Valette R, Karbou F, Morin S. 2013. Simulation of northern Eurasian local snow depth, mass and density using a detailed snowpack model and meteorological reanalyses. *J. Hydrometeorol.* **14**: 203–219.
- Bulygina ON, Groisman PY, Razuvaev VN, Korshunova NN. 2011. Changes in snow cover characteristics over Northern Eurasia since 1966. *Environ. Res. Lett.* **6**: 045026.
- Cassano EN, Lynch AH, Cassano JJ, Koslow MR. 2006. Classifications of synoptic patterns in the western Arctic associated with extreme events at Barrow, Alaska. *Clim. Res.* **30**: 83–97.
- Cassou C. 2008. Intraseasonal interaction between the Madden-Julian oscillation and the North Atlantic Oscillation. *Nature* **455**: 523–527.
- Cavazos T. 1999. Large-scale circulation anomalies conducive to extreme precipitation events and derivation of daily rainfall in northeastern Mexico and southeastern Texas. *J. Clim.* **12**: 1506–1523.
- Cavazos T. 2000. Using self-organizing maps to investigate extreme climate events: an application to wintertime precipitation in the Balkans. *J. Clim.* **13**: 1718–1732.
- Cohen J, Entekhabi D. 1999. Eurasian snow cover variability and Northern Hemisphere climate predictability. *Geophys. Res. Lett.* **26**: 345–348.
- Cohen J, Jones J. 2011. A new index for more accurate winter predictions. *Geophys. Res. Lett.* **38**: L21701.
- Cohen J, Barlow M, Kushner PJ, Saito K. 2007. Stratosphere–troposphere coupling and links with Eurasian land surface variability. *J. Clim.* **20**: 5335–5343.
- Derksen C, LeDrew E. 2000. Variability and change in terrestrial snow cover: data acquisition and links to the atmosphere. *Prog. Phys. Geogr.* **24**: 496–498.
- Dye DG. 2002. Variability and trends in the annual snow-cover cycle in Northern Hemisphere land areas, 1972–2000. *Hydrol. Processes* **16**: 3065–3077.
- Estilow TW, Young AH, Robinson DA. 2015. A long-term Northern Hemisphere snow cover extent data record for climate studies and monitoring. *Earth Syst. Sci. Data* **7**: 137–142.
- Falarz M. 2013. Seasonal stability of snow cover in Poland in relation to the atmospheric circulation. *Theor. Appl. Climatol.* **111**: 21–28.
- Fassnacht SR, Derry JE. 2010. Defining similar regions of snow in the Colorado River Basin using self-organizing maps. *Water Resour. J.* **46**: W04507.
- Flatau M, Kim YJ. 2013. Interaction between the MJO and polar circulations. *J. Clim.* **26**: 3562–3574.
- Fletcher CG, Kushner PJ, Cohen J. 2007. Stratospheric control of the extratropical circulation response to surface forcing. *Geophys. Res. Lett.* **34**: L21802.
- Furtado JC, Cohen J, Butler AH, Riddle EE, Kumar A. 2015. Eurasian snow cover variability and links to winter climate in the CMIP5 models. *Clim. Dyn.*, **45**(9): 2591–2605, doi: 10.1007/s00382-015-2494-4.
- Gong G, Entekhabi D, Cohen J. 2003. Modeled Northern Hemisphere winter climate response to realistic Siberian snow anomalies. *J. Clim.* **16**: 3917–3931.
- Hardiman SC, Kushner PJ, Cohen J. 2008. Investigating the ability of general circulation models to capture the effects of Eurasian snow cover on winter climate. *J. Geophys. Res. Atmos.* **113**: D21123, doi: 10.1029/2008JD010623.
- Haykin S. 1994. *Neural Networks. A Comprehensive Foundation*. Macmillan: New York, NY, 837 pp.
- Henderson GR, Leathers DJ. 2010. European snow cover extent variability and associations with atmospheric forcings. *Int. J. Climatol.* **30**: 1440–1451.
- Henderson GR, Barrett BS, LaFleur DM. 2014. Arctic sea ice and the Madden-Julian Oscillation (MJO). *Clim. Dyn.* **43**: 2185–2196.
- Johnson NC, Feldstein SB. 2010. The continuum of North Pacific sea level pressure patterns: intraseasonal, interannual, and interdecadal variability. *J. Clim.* **23**: 851–867.
- Kohonen T. 1988. *Self-Organization and Associative Memory*. Springer-Verlag: New York, NY and Berlin and Heidelberg, Germany.
- Kohonen T. 2001. *Self-Organizing Maps*. Springer-Verlag: New York, NY and Berlin and Heidelberg, Germany.
- L'Heureux ML, Higgins RW. 2008. Boreal winter links between the Madden-Julian Oscillation and the Arctic Oscillation. *J. Clim.* **21**: 3040–3050.
- LaFleur DM, Barrett BS, Henderson GR. 2015. Some climatological aspects of the Madden-Julian Oscillation (MJO). *J. Clim.* **28**: 6039–6053.
- Lin H, Brunet G. 2009. The influence of the Madden-Julian Oscillation on Canadian wintertime surface air temperature. *Mon. Weather Rev.* **137**: 2250–2262.
- Liu Y, Weisberg HR. 2005. Patterns of ocean current variability on the West Florida Shelf using the self-organizing map. *J. Geophys. Res.* **110**: C06003, doi: 10.1029/2004JC002786.
- Liu Y, Weisberg RH. 2011. A review of self-organizing map applications in meteorology and oceanography. In *Self Organizing Maps – Applications and Novel Algorithm Design*. Mwasigani JI (ed). InTech Publishers: Rijeka, Croatia, 253–272.
- Madden RA, Julian PR. 1971. Detection of a 40–50 day oscillation in the zonal wind in the tropical Pacific. *J. Atmos. Sci.* **28**: 702–708.
- Madden RA, Julian PR. 1972. Description of global-scale circulation cells in the tropics with a 40–50 day period. *J. Atmos. Sci.* **29**: 1109–1123.
- Matthews AJ, Hoskins BJ, Masutani M. 2004. The global response to tropical heating in the Madden-Julian Oscillation during Northern winter. *Q. J. R. Meteorol. Soc.* **130**: 1991–2011.
- Mudryk LR, Derksen C, Kushner P, Brown R. 2015. Characterization of northern hemisphere snow water equivalent datasets, 1981–2010. *J. Clim.* **28**: 8037–8051.
- Peings Y, Saint Martin D, Douville H. 2012. A numerical sensitivity study of the influence of Siberian snow on the Northern Annular Mode. *J. Clim.* **25**: 592–607.
- Peng S, Piao S, Ciais P, Friedlingstein P, Zhou L, Wang T. 2013. Change in snow phenology and its potential feedback to temperature in the Northern Hemisphere over the last three decades. *Environ. Res. Lett.* **8**: 014008.
- Richardson AJ, Risien C, Shillington FA. 2003. Using self-organizing maps to identify patterns in satellite imagery. *Prog. Oceanogr.* **59**: 223–239.
- Sardeshmukh PD, Hoskins BJ. 1988. The generation of global rotational flow by steady idealized tropical divergence. *J. Atmos. Sci.* **45**: 1228–1251.
- Skific N, Francis J. 2012. Self-organizing maps: a powerful tool for the atmospheric sciences. In *Developments and Applications of*

- Self-Organizing Maps*, Johnsson M (ed). InTech, ISBN: 978-953-51-0862-7, doi: 10.5772/54299. <http://www.intechopen.com/books/applications-of-self-organizing-maps/self-organizing-maps-a-powerful-tool-for-the-atmospheric-sciences> (accessed 24 July 2014).
- Smith KL, Kushner PJ, Cohen J. 2011. The role of linear interference in northern annular mode variability associated with Eurasian snow cover extent. *J. Clim.* **24**: 6185–6202.
- Takala M, Pulliainen J, Huttunen M, Hallikainen . 2008. Detecting the onset of snow-melt using SSM/I data and the self-organizing map. *Int. J. Remote Sens.* **29**: 755–766.
- Thompson JA, Lees BG. 2014. Applying object-based segmentation in the temporal domain to characterize snow seasonality. *ISPRS J. Photogramm. Remote Sens.* **97**: 98–110.
- Thompson D, Wallace J. 1998. The Arctic Oscillation signature in the wintertime geopotential height and temperature fields. *Geophys. Res. Lett.* **25**: 1297–1300.
- Tian B, Fan K. 2015. A skillful prediction model for winter NAO based on Atlantic sea surface temperature and Eurasian snow cover. *Weather Forecast.* **30**: 197–205.
- Vernekar AD, Zhou J, Shukla J. 1995. The effect of Eurasian snow cover on the Indian monsoon. *J. Clim.* **8**: 248–266.
- Vesanto J, Alhoniemi E. 2000. Clustering of the self-organizing map. *IEEE Trans. Neural Networks* **11**: 586–600.
- Wheeler M, Hendon HH. 2004. An all-season real-time multivariate MJO index: development of an index for monitoring and prediction. *Mon. Weather Rev.* **123**: 1917–1932.
- Wu R, Liu G, Ping Z. 2014. Contrasting Eurasian spring and summer climate anomalies associated with western and eastern Eurasian spring snow cover changes. *J. Geophys. Res. Atmos.* **119**: 7410–7424, doi: 10.1002/2014JD021764.
- Xia K, Wang B, Li L, Shen S, Huang W, Xu S, Dong L, Liu L. 2014. Evaluation of snow depth and snow cover fraction simulated by two versions of the flexible global ocean-atmosphere-land system model. *Adv. Atmos. Sci.* **31**: 407–420, doi: 10.1007/s00376-013-3026-y.
- Yoo C, Lee S, Feldstein SB. 2012. Mechanisms of Arctic surface air temperature change in response to the Madden–Julian Oscillation. *J. Clim.* **25**: 5777–5790.